nature communications

Article

https://doi.org/10.1038/s41467-026-68283-w

# Magneto-ionic control of magnetism through voltage-driven carbon transport

Received: 25 March 2025

Accepted: 29 December 2025

Published online: 13 January 2026

Check for updates

Z. Tan[1,2,3] ✉, Z. Ma[3] ✉, S. Privitera[3,4], M. O. Liedke[5], E. Hirschmann[5], A. Wagner[5], J. L. Costa-Krämer[6], A. Quintana[3,4], A. Garcia-Tort[7], J. Herrero-Martín[7], Y. F. Mei[1,2], X. Z. Chen[1,2], H. Tan[3,4], I. Fina[8], F. Sánchez[8], A. Arredondo-López[3], F. Ibrahim[9], M. Chshiev[9,10], E. Longo[8], M. Rovirola[11,12], F. Macià[11,12], A. F. Lopeandia[3,4], J. Nogués[4,13], E. Pellicer[3], J. Sort[3,4,13] ✉ & E. Menéndez[3] ✉

Control of magnetism through voltage-driven ionic processes (*i.e.*, magneto-ionics) holds potential for next-generation memories and computing. This stems from its non-volatility, flexibility in adjusting the magnitude and speed of magnetic modulation, and energy efficiency. Since magneto-ionics depends on factors like ionic radius and electronegativity, identifying alternative mobile ions is crucial to embrace new phenomena and applications. Here, the feasibility of C as a prospective magneto-ionic ion is investigated in a Fe-C system by electrolyte gating. In contrast to most magneto-ionic systems, Fe-C presents a reversible dual-ion mechanism: Fe and C act as cation and anion, respectively, moving uniformly in opposite directions under an applied electric field. This leads to a significant increase in saturation magnetization ( > 5-fold) with magneto-ionic rates larger than 1 emu·cm$^{-3}$·s$^{-1}$, and a 25-fold increase in coercivity. Since carbides exhibit minimal cytotoxicity, this introduces a biocompatible dimension to magneto-ionics, paving the way for the convergence of spintronics and biotechnology.

Magneto-ionics, which deals with the control of magnetic properties through voltage-driven ionic transport and/or redox processes, is gaining momentum as a magneto-electric mechanism for low-power spintronics[1]. The appeal lies in its non-volatility, enabled by its electrochemical character[2], and its versatility in tuning the degree and speed of magnetic modulation. This is attractive for a broad range of applications, such as neuromorphic computing[3], and data encryption[4]. The diverse responses exhibited by magneto-ionic systems depend on the mobile species (e.g., $H^{+5}$, $Li^{+6}$, $O^{2-8}$, $F^{-9}$, $OH^{-10}$, or $N^{3-11-13}$), the phase and/or stoichiometry of the actuated material, and the magnetic property (*e.g.*, magnetic anisotropy[5,7], coercivity, $H_C$[14], or saturation magnetization, $M_S$[8,11,12]) used to track the magneto-ionic response.

[1]Zhejiang Key Laboratory of Extreme Environment Functional Materials, Yiwu Research Institute of Fudan University, Yiwu, People's Republic of China. [2]International Institute for Intelligent Nanorobots and Nanosystems, College of Intelligent Robotics and Advanced Manufacturing, State Key Laboratory of Photovoltaic Science and Technology, Shanghai Frontiers Science Research Base of Intelligent Optoelectronics and Perception, Institute of Optoelectronics, State Key Laboratory of Surface Physics, Fudan University, Shanghai, China. [3]Departament de Física, Universitat Autònoma de Barcelona, Cerdanyola del Vallès, Spain. [4]Catalan Institute of Nanoscience and Nanotechnology (ICN2), CSIC and BIST, Campus UAB, Bellaterra, 08193, Barcelona, Spain. [5]Institute of Radiation Physics, Helmholtz-Zentrum Dresden – Rossendorf, Dresden, Germany. [6]IMN-Instituto de Micro y Nanotecnología (CNM-CSIC), Isaac Newton 8, PTM, Tres Cantos, Madrid, Spain. [7]ALBA Synchrotron Light Source, Cerdanyola del Vallès, Spain. [8]Institut de Ciencia de Materials de Barcelona, ICMAB-CSIC, Campus UAB, Bellaterra, Barcelona, Spain. [9]Univ. Grenoble Alpes, CEA, CNRS, Spintec, Grenoble, France. [10]Institut Universitaire de France (IUF), Paris, France. [11]Departament de Física de la Matèria Condensada, Facultat de Física, Universitat de Barcelona, Barcelona, Spain. [12]Institut de Nanociència i Nanotecnologia (IN2UB), Universitat de Barcelona, Barcelona, Spain. [13]Institució Catalana de Recerca i Estudis Avançats (ICREA), Pg. Lluís Companys 23, Barcelona, Spain. ✉e-mail: tanzw@ywfudan.cn; ma.zheng@uab.cat; jordi.sort@uab.cat; enric.menendez@uab.cat

Despite significant progress in this area, the number of materials exhibiting magneto-ionics remains limited. Since magneto-ionics critically depends on the synergy of different parameters, such as the ionic radius, electronegativity, or diffusivity, the search for additional magneto-ionic materials and mobile ion species is essential to enable new phenomena and innovative applications.

Here, we demonstrate simultaneous voltage-driven C and Fe ion transport as an approach to modulate ferromagnetism in Fe-C-based heterostructures. This transport occurs uniformly, resembling a planar front, with C and Fe moving in opposite directions, behaving as cation and anion, respectively, due to their electronegativity difference. Voltage actuation results in a significant enhancement ( > 5-fold) in $M_S$ and a 25-fold increase in $H_C$, with a magneto-ionic rate larger than 1 emu·cm$^{-3}$·s$^{-1}$. This combination of features sets the stage for innovative uses of magneto-ionic systems and highlights the importance of investigating alternative mobile cations and anions to broaden the functionalities and applications of magneto-ionics.

## Results and discussion

The as-prepared Fe-C film comprises a heterostructure which consists of four Fe-C layers of different compositions capped by a Ti-C layer, as shown schematically in Fig. 1a. The rationale behind the design of the heterostructure is to enable and maximize magneto-ionic effects through voltage-driven Fe and C transport in Fe-C systems (see Supplementary Section 1 and Supplementary Fig. S1 for details on the fabrication and compositional/structural characterization of the as-prepared heterostructure, which primarily consists of a thermal treatment, and Supplementary Fig. S2 for the voltage actuation protocol). In contrast to the as-grown sample, which consists of a ferromagnetic Fe-rich phase embedded in a C-rich matrix (Supplementary Section 1), the as-prepared heterostructure is weakly magnetic, with a $M_S$ of 169 emu·cm$^{-3}$ and a $H_C$ of 11 Oe (compare Fig. 1b with Supplementary Fig. S1d). Therefore, the annealing is consistent with the carburization of the Fe-rich phase, resulting in paramagnetic iron carbides, like hexagonal $Fe_2C$[15], and/or ferromagnetic iron carbides, such as $Fe_7C_3$ and $Fe_3C$, with $M_S$ values of 120 and 125 emu·g$^{-1}$[16], respectively (taking 7.82[17] and 7.662 g·cm$^{-3}$[18] as densities for $Fe_7C_3$ and $Fe_3C$, the $M_S$ values in emu·g$^{-1}$ transform into 938.4 and 957.8 emu·cm$^{-3}$, respectively), significantly lower than that of body-centered cubic (BCC) Fe (217.3 emu·g$^{-1}$, which transforms into 1711.4 emu·cm$^{-3}$ upon taking 7.874 g·cm$^{-3}$ as density)[19]. In addition, the as-prepared films exhibit moderate resistivity (Supplementary

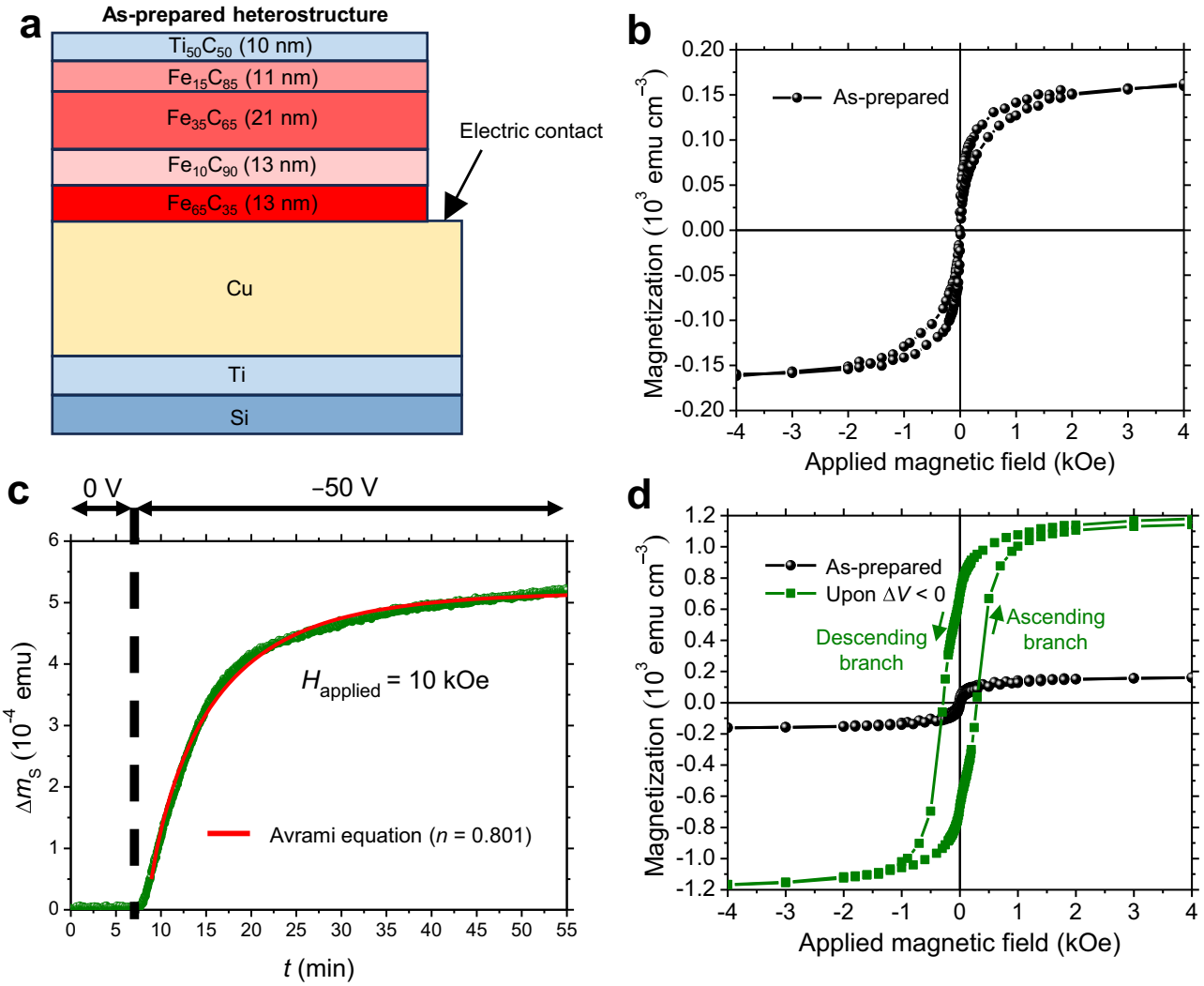


**Fig. 1 | Magneto-ionic response of the as-prepared heterostructure. a** Schematic illustration of the cross-section of the as-prepared heterostructure. **b** Hysteresis loop of an as-prepared heterostructure. **c** Dependence of the generated magnetic moment at saturation (*i.e.*, $\triangle m_S$) as a function of time ($t$) while applying − 50 V. The experimental datapoints are fitted to an Avrami equation (Eq. (1)). **d** Hysteresis loops of the as-prepared sample (shown in panel **b**), and after being actuated with − 50 V for 1 h. The magnetic field was swept from 20 kOe to − 20 kOe and back, and the arrows indicate descending and ascending branches. The magnetization in panels (**b**, **d**) is normalized to the volume of the Fe-containing layers (see Methods).

Section 2 and Supplementary Fig. S3), which makes the system suitable for voltage actuation through magneto-ionics[12]. Fig. 1c shows the evolution of the change in magnetic moment at saturation (see Methods, Supplementary Fig. S4 and Supplementary Section 3 for the justification of the use of magnetic moment), $\triangle m_S(t)$, while applying a gating voltage of − 50 V. At the early stages of voltage actuation, the generated magnetic moment increases rapidly and linearly, evidencing strong magneto-electric effects which could be compatible with C and/or Fe ionic transport. Considering the layered structure of the as-prepared film, the electric field actuation perpendicular to the film, and the initial linear dependence of the generated magnetic moment at saturation with time (i.e., $\triangle m_S(t) \propto t$), interface-controlled ionic transport is envisaged[20]. With further gating time, this growth levels off until it reaches a steady state. To shed more light on ion mobility mechanisms, the data in Fig. 1c was fitted to the following Avrami formalism[20]:

$$\triangle m_S(t) = \triangle m_S^{t\to\infty}\left(1 - e^{-k(t-t_0)^n}\right) \quad (1)$$

where $\triangle m_S^{t\to\infty}$ is the generated long-term magnetic moment at saturation ($\triangle m_S^{t\to\infty} = (5.170 \pm 0.006)\,10^{-4}$ emu), $k$ an overall rate constant ($k = 0.215 \pm 0.003$), $n$ the Avrami exponent ($n = 0.801 \pm 0.006$), and $t_0$ the time in which the voltage was set ON ($t_0 = 8.54 \pm 0.02$ min). An $n$ lower than one is typically associated with heterogeneous nucleation and restricted growth processes[20]. However, the fit, with an adjusted $R^2$ of 0.9981, does not completely align with the experimental data, indicating that there may be different ion motion mechanisms over the extended voltage actuation periods. As shown in Supplementary Fig. S5, when the Avrami formalism was applied to the generated magnetic moment data from the first minutes of voltage actuation, the goodness-of-fit, with $R^2$ of 0.9998, improves considerably. An Avrami exponent of $n = 1.296 \pm 0.008$ is determined, indicating the presence of a distinct ion motion mechanism in the early stages of the magneto-ionic process, which goes beyond one-dimensional motion, suggesting a two-dimensional motion (plate-like growth)[20], as seen in nitride-based systems[11]. To estimate the magneto-ionic rate, which accounts for the change in generated magnetization with time, in the first stages of the gating, the initial slope of Fig. 1c curve is normalized to the volume of the as-prepared sample, resulting in values larger than 1 emu·cm$^{-3}$·s$^{-1}$. This value is comparable to the performance of nitrogen magneto-ionics and surpasses that of oxygen magneto-ionics[8]. After applying a negative bias of −50 V for 1 h, the voltage was turned off, and a hysteresis loop was recorded by vibrating sample magnetometry (Fig. 1d). The ascending branch of the loop shows a slightly lower $M_S$ (around 2 %) compared to the descending branch, which could be compatible with a partial magnetization depletion due to a mild recarburization process. Despite this, the voltage-induced ferromagnetic changes are significant and largely permanent. Upon voltage actuation, $M_S$ and $H_C$ increase from 169 to 1176 emu·cm$^{-3}$ and from 11 to 294 Oe, respectively (Fig. 1d). This enhancement in saturation magnetization upon voltage actuation is consistent with the formation of metallic iron and Fe-rich phases, aligning with voltage-driven Fe and/or C ion transport processes that decarburize certain regions of the film. Furthermore, the increase in coercivity from 11 to 294 Oe after voltage actuation (Fig. 1d) is compatible with the formation of ferromagnetic Fe clusters[21] surrounded by Fe carbides, since $H_C$ is proportional to the volume of magnetic material above the superparamagnetic limit and below the critical single-domain size[19,22], and more stoichiometric $Fe_3C$[23].

To exclude volume normalization as the origin of the voltage-driven magnetic modulation, the hysteresis loops of all heterostructures were plotted as magnetic moment ($m$) *vs.* applied magnetic field, as shown in Supplementary Fig. S6. Since all samples were prepared from identical as-grown samples, the observed changes in magnetization, which resemble those of magnetic moment (compare Fig. 1 with Supplementary Fig.S6), can be attributed to voltage-driven Fe and C ion migration effects. The magnetic anisotropy of the different samples was assessed by angular-dependent vibrating sample magnetometry measurements (Supplementary Figs. S7 and S8) and ferromagnetic resonance characterization (Figure S9). As shown in Supplementary Fig. S7b, e, h, the as-grown films are ferromagnetically soft (*i.e.*, low coercivity) due to the presence of Fe, exhibiting a slight in-plane uniaxial anisotropy with the hard axis aligned along the film's longest dimension (*i.e.*, a constriction at 90 degree of the polar plot of the squareness). In the as-prepared state (after annealing, see Supplementary Fig. S7c, f, i), ferromagnetism is reduced (see the reduction of the magnetic moment at saturation upon thermal treatment in Supplementary Fig. S6a), while the films become magnetically harder (the coercivity increases approximately from 2 to 33 Oe upon annealing) because of the formation of iron carbides. The magnetic behavior becomes isotropic in the plane of the sample, and the observed constriction of the hysteresis loops (Supplementary Fig. S7c) is attributed to dipolar interactions among more isolated ferromagnetic regions, consistent with the carburization of Fe, forming iron carbides and leaving the ferromagnetic counterparts more apart, as happens in prior reports on similar scenarios. Upon voltage actuation (− 50 V for 1 h), ferromagnetism is virtually restored, as evidenced by the recovery of the magnetic moment at saturation (Supplementary Fig. S6b, c and Fig. 1b, d), and the films become even more magnetically hard (reaching coercivities above 300 Oe) with an isotropic in-plane behavior. Such an increase might be ascribed to the formation of ferromagnetic clusters[24]. In contrast to the as-prepared heterostructure, the hysteresis loops no longer display a central constriction, indicating that the ferromagnetic regions have evolved upon gating into continuous networks where exchange interactions dominate over dipolar ones[24,25]. Together, these magnetic results are consistent with the generation of ferromagnetism by voltage-driven dual and opposite ion transport of Fe and C. The out-of-plane magnetic response is assessed by performing hysteresis loops from in-plane (0 degree) to intermediate (45 degree) and out-of-plane (90 degree) configurations. Only the as-grown sample (Supplementary Fig. S8a) shows a well-defined out-of-plane component, consistent with the presence of ultrathin Fe counterparts and in agreement with earlier reports on ultrathin films[26]. After annealing, the out-of-plane direction becomes a clear hard axis (Supplementary Fig. S8b), reflecting in-plane magnetic anisotropy dominated by shape effects due to the layered heterostructure (as detailed below in Fig. 2a, b). Upon voltage actuation (−50 V for 1 h), the out-of-plane direction remains a hard axis (Supplementary Fig. S8c), again due to shape anisotropy, but now associated with Fe-rich phases reorganized into a continuous single layer (as detailed below in Fig. 2c, d). Taken together, both in-plane and out-of-plane characterizations reveal that voltage actuation results in no significant change of magnetic anisotropy. To quantify the magnetic anisotropy of the heterostructure subjected to voltage actuation, broadband ferromagnetic resonance spectroscopy was carried out on the heterostructure biased at − 50 V for 1 h (see below). The results indicate that the shape and volume anisotropy constants are similar, further confirming the in-plane magnetic anisotropy of the heterostructure subjected to voltage actuation. Supplementary Fig. S9 shows the Kittel dispersion for the − 50 V-gated sample acquired while maintaining a quasi-static external magnetic field ($H_{ext}$) parallel to the sample surface (*i.e.*, in-plane configuration), where the resonant frequency ($f_{res}$) is plotted as a function of the resonant magnetic field ($H_{res}$), black circles. The red solid line represents the fit of the dataset with the Kittel equation for in-plane magnetized polycrystalline ferromagnetic thin films, as described by Eq. (2):

$$f_{res} = \frac{\gamma}{2\pi}\sqrt{H_{res}\left(H_{res} + 4\pi M_{eff}\right)} \quad (2)$$

where $M_{eff}$ is the effective magnetization, $\gamma = g\frac{e}{2m_e}$ Hz·Oe$^{-1}$ is the gyromagnetic ratio, with $e$ and $m_e$ are the charge and the mass of the electron, respectively, and $g$ is the Landé g-factor[27]. In order to minimize the fitting error, $\gamma$ is fixed to $1.88 \times 10^7$ Hz·Oe$^{-1}$, a typical value for Fe thin films corresponding to $g = 2.14$[28]. Accordingly, the extracted $M_{eff}$ is $364 \pm 5$ emu·cm$^{-3}$. $M_{eff}$ accounts for the magnetic anisotropy in the ferromagnetic Fe-rich layer (*i.e.*, area VI of Fig. 2c, d), and it can be expressed as $4\pi M_{eff} = 4\pi M_S - H_{eff} \propto 4\pi M_S - \frac{2K_{eff}}{M_S}$, where $H_{eff}$ and $K_{eff}$ are the effective magnetic anisotropy field and constant, respectively[27]. The effective anisotropy can be further decomposed as $K_{eff} = K_V + \frac{2K_S}{M_S t_{Fe-rich\ layer}}$, where $K_V$, $K_S$ and $t_{Fe-rich\ layer}$ are the volume anisotropy constant, surface anisotropy constant and ferromagnetic layer thickness, respectively[27]. For thick films $K_S \approx 0$, thus the most relevant contribution to the out-of-plane anisotropy is due to $K_V$. According to that and using $M_S = 1176$ emu·cm$^{-3}$, $K_{eff} \approx K_V = 6.0 \times 10^6$ erg·cm$^{-3}$, a value typical for Fe thin films[29]. To assess the relative magnitude of the in-plane anisotropy, we calculated the shape anisotropy constant as $K_{shape} = -\frac{1}{2}\mu_0 M_s^2 = -8.7 \times 10^6$ erg·cm$^{-3}$. Since $K_{shape}$ is like $K_{eff}$ in absolute value, this indicates that the film is primarily in-plane magnetized.

Supplementary Fig. S10 schematically summarizes the ion reconfiguration mechanisms involved in C-based magneto-ionics. Under sample preparation (*i.e.*, annealing), the decrease in magnetic moment (or magnetization) is driven by thermally induced formation of iron carbides, while the increase upon biasing is linked to the opposing effect (*i.e.*, voltage-driven transport of Fe and C ionic species, resulting in the formation of ferromagnetic BCC Fe-rich regions, likely emerging through the sequential phase transformation: $Fe_2C \rightarrow Fe_7C_3 \rightarrow Fe_3C \rightarrow$ BCC-Fe). Among iron carbides, there are paramagnetic, such as hexagonal $Fe_2C$[15], and ferromagnetic, such as $Fe_7C_3$ and $Fe_3C$, phases. The latter exhibit $M_S$ values of 938.4 and 957.8 emu·cm$^{-3}$ [16], showing significantly lower $M_S$ than BCC-Fe (1711.4 emu·cm$^{-3}$)[19]. The formation of iron oxides can be disregarded because the Ti-C overlayer acts as a protective barrier. In fact, if oxygen were present, it would drive carbon into a positive oxidation state due to its much higher electronegativity. This state would cause carbon ions to migrate downward under negative bias, a behavior not observed experimentally, further confirming the protecting role of the Ti-C layer. Therefore, the presence of iron oxides within the interior of the heterostructure can be ruled out, and thus their influence on the observed magnetic changes can also be excluded.

To validate the hypothesis of voltage-driven ion motion of Fe and/or C in a planar-like front, a high-angle annular dark-field scanning transmission electron microscopy (HAADF-STEM)/elemental electron energy loss spectroscopy (EELS) characterization of an as-prepared sample and a sample treated with − 50 V for 1 h was carried out (Fig. 2). Energy-dispersive X-ray spectroscopy (EDX) characterization shows a four-layer structure in the as-prepared state, consisting of $Fe_{15}C_{85}$ (Area I), $Fe_{35}C_{65}$ (Area II), $Fe_{10}C_{90}$ (Area III), and $Fe_{65}C_{35}$ (Area IV) layers from top to bottom. When voltage is applied, the original multilayer structure (with four distinct Fe-C layers) transforms into a bilayer, where the bottom layer, which resembles the bottom layer of the as-prepared sample from compositional and microstructural viewpoints, becomes thicker (Supplementary Figs. S11 and S12 for further information on microstructural aspects). When comparing the composition of the as-prepared and − 50 V-gated samples, a well-defined trend of ion diffusion is manifested. The voltage-induced top layer (Area V) is virtually Fe-free and is of the same thickness as the sum of thickness of Area I, Area II, and Area III of the as-prepared sample, while the voltage-induced bottom layer (Area VI) becomes thicker than Area IV with a richer composition in Fe: $Fe_{80}C_{20}$. These results clearly evidence that the voltage induces dual-ion motion, where Fe and C move in opposite directions. Namely, C, being more electronegative than Fe, moves upwards (towards the counter electrode, which is positively polarized with respect to the Cu bottom electrode, Supplementary Fig. S2), whereas Fe migrates downwards. Moreover, after biasing, the Ti-C layer becomes richer in C (*i.e.*, $Ti_{50}C_{50}$ *vs.* $Ti_{40}C_{60}$ for the as-prepared and voltage-treated samples, respectively), further confirming the voltage-driven C transport towards the upper part (*i.e.*, to the Ti-C reservoir).

To unravel the crystalline order, high-resolution transmission electron microscopy (HR-TEM) imaging was carried out (Supplementary Figs. S11 and S12). The C-rich layers (*i.e.*, Area I, Area II, Area III −as-prepared sample−, and Area V −voltage-treated sample−) are amorphous-like (see Supplementary Fig. S11 in which a diffuse halo and no rings nor spots are observed in the fast Fourier transform, FFT, images), while the others (*i.e.*, Area IV −as-prepared− and Area VI −voltage-treated−) exhibit some degree of crystallinity (Supplementary Fig. S12). FFTs reveal Fe carbide formation in the form of $Fe_2C$ and $Fe_3C$ in Area IV of the as-prepared heterostructure. The interplanar distances are slightly shifted towards lower values, confirming the formation of non-stoichiometric Fe carbides, as envisaged from the magnetometry results. With voltage, slightly more polycrystalline $Fe_2C$ and $Fe_3C$ phases form, since more diffraction spots appear, and spot #3 in Fig. S12 is likely arising mainly from metallic Fe, revealing the effect of Fe and C transport on the microstructure (Supplementary Fig. S12). The presence of oxide traces is mainly linked to natural oxidation of the prepared lamellae.

The evolution of the defect microstructure as a function of depth was determined by variable energy positron annihilation lifetime spectroscopy (VEPALS). As seen in Fig. 3, the main changes in the VEPALS occur in the bottom layer of the gated samples (Area VI). The average positron lifetime clearly decreases upon voltage actuation, indicating smaller average defect sizes, in concordance with the enhanced crystallinity and increased thickness of Area VI (23 nm) compared to Area IV (13 nm) (see Supplementary Figs. S4, S11, S12). The estimated major defect size (*i.e.*, $\tau_1$) reduces from the range of bi-vacancy for as-prepared samples to the single vacancy in the case of the biased sample (Fig. 3b). In addition, vacancy agglomerations (*i.e.*, $\tau_2$), originating from the amorphous-like counterparts, are found, undergoing a strong reduction in size from ≈ 16 to ≈ 12 vacancies within the vacancy complex upon voltage actuation (Fig. 3b). See Methods and Supplementary Section 4 for further details on the VEPALS characterization.

Remarkably, the HR-TEM and VEPALS results seem to indicate not only an ion movement, but an unprecedented partial voltage-induced recrystallization of some of the amorphous layers in the system.

To gain more insight into the compositional aspects, X-ray absorption spectroscopy (XAS) measurements were performed, in both total electron yield (TEY) and fluorescence yield (FY) modes (Supplementary Fig. S13). Total electron yield (TEY) characterizes the oxidation state of the first top nanometers, while fluorescence yield (FY) provides insights into much deeper parts (*i.e.*, several tens of nm)[30]. Supplementary Fig. S13a presents the Fe $L_{2,3}$-edge XAS spectra for the as-prepared, and voltage-treated with − 50 V for 5 min heterostructures. The as-prepared sample spectra reveal characteristic peaks at around 707.3 and 708.8 eV at the $L_3$ edge, compatible with $Fe^{2+}$ and $Fe^{3+}$ which are linked to iron carbide formation, in agreement with the high-resolution TEM results (Supplementary Fig. S12). Upon voltage actuation, the spectra undergo noticeable changes, as highlighted in Supplementary Fig. S13b. Interestingly, the $L_3/L_2$ ratio decreases in TEY mode, whereas it increases in FY mode. Since the $L_3/L_2$ ratio is inversely proportional to the degree of carburization (*i.e.*, to the C/Fe ratio)[31], this indicates an increased C/Fe ratio at the film surface with respect to the rest of the heterostructure, confirming the voltage-driven dual motion of C (upwards) and Fe (downwards).

As seen in Fig. 4a, after a reverse actuation process, by applying +50 V for 1 h (data in blue), a depletion of $M_S$ down to 845 emu·cm$^{-3}$ occurs, evidencing partial reversibility, similar to what happens in other magneto-ionic systems, such as in $Co_3O_4$[8,32]. Upon reverse

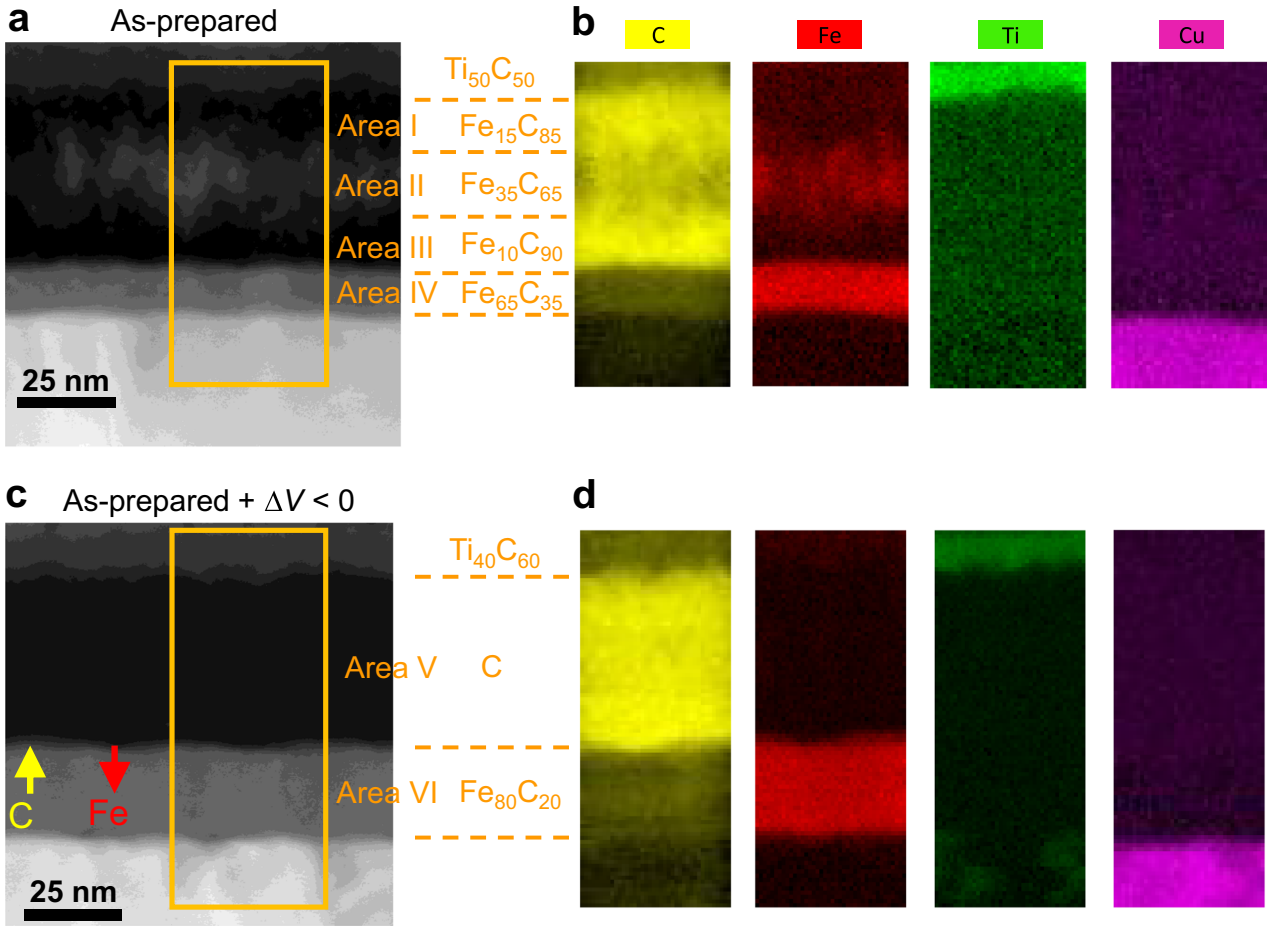


**Fig. 2 | Compositional characterization of as-annealed and voltage-actuated heterostructures. a** HAADF-STEM micrograph of a cross-section of an as-prepared sample. **b** C, Fe, Ti, and Cu elemental EELS mappings of the region marked with a yellow rectangle in panel (**a**). **c** HAADF-STEM micrograph of a cross-section of a sample treated with −50 V for 1 h. **d** C, Fe, Ti, and Cu elemental EELS mappings of the region marked with a yellow rectangle in panel (**c**).

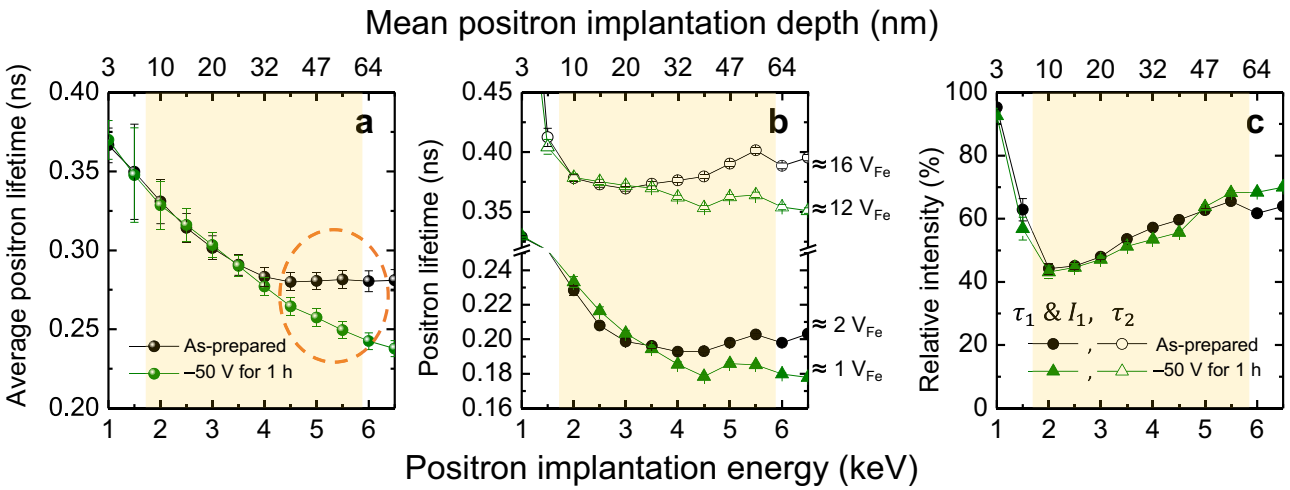


**Fig. 3 | Defect characterization by VEPALS. a** Average positron lifetime. **b** Positron lifetime components (*i.e.*, $\tau_1$ and $\tau_2$), and **c** the relative intensities of defects characterized by $\tau_1$ (*i.e.*, $I_1$) as a function of positron implantation energy (*i.e.*, mean positron implantation depth, see Methods) of the as-prepared and voltage-treated heterostructures. The orange background approximates the Fe-C film region (see "Methods"), and the orange dashed-line mainly embraces the results corresponding to Area IV of the as-prepared sample and Area VI of the voltage-treated one. $V_{Fe}$ stands for iron vacancy.

actuation, besides the decrease in $M_S$, $H_C$ and $M_R$ remain unchanged, consistent with a uniform, planar-like transport of C (downwards) and Fe (upwards) ions, causing Fe carburization, and forming Fe carbides with lower $M_S$ than Fe. To magnetically restore the as-prepared state, the sample must be annealed (data in orange), replicating the effects of the initial annealing process of the as-grown film, to allow sufficient Fe and C diffusion and thus form Fe carbides. Ab initio calculations support these observations (Supplementary Fig. S14), showing that the

https://doi.org/10.1038/s41467-026-68283-w

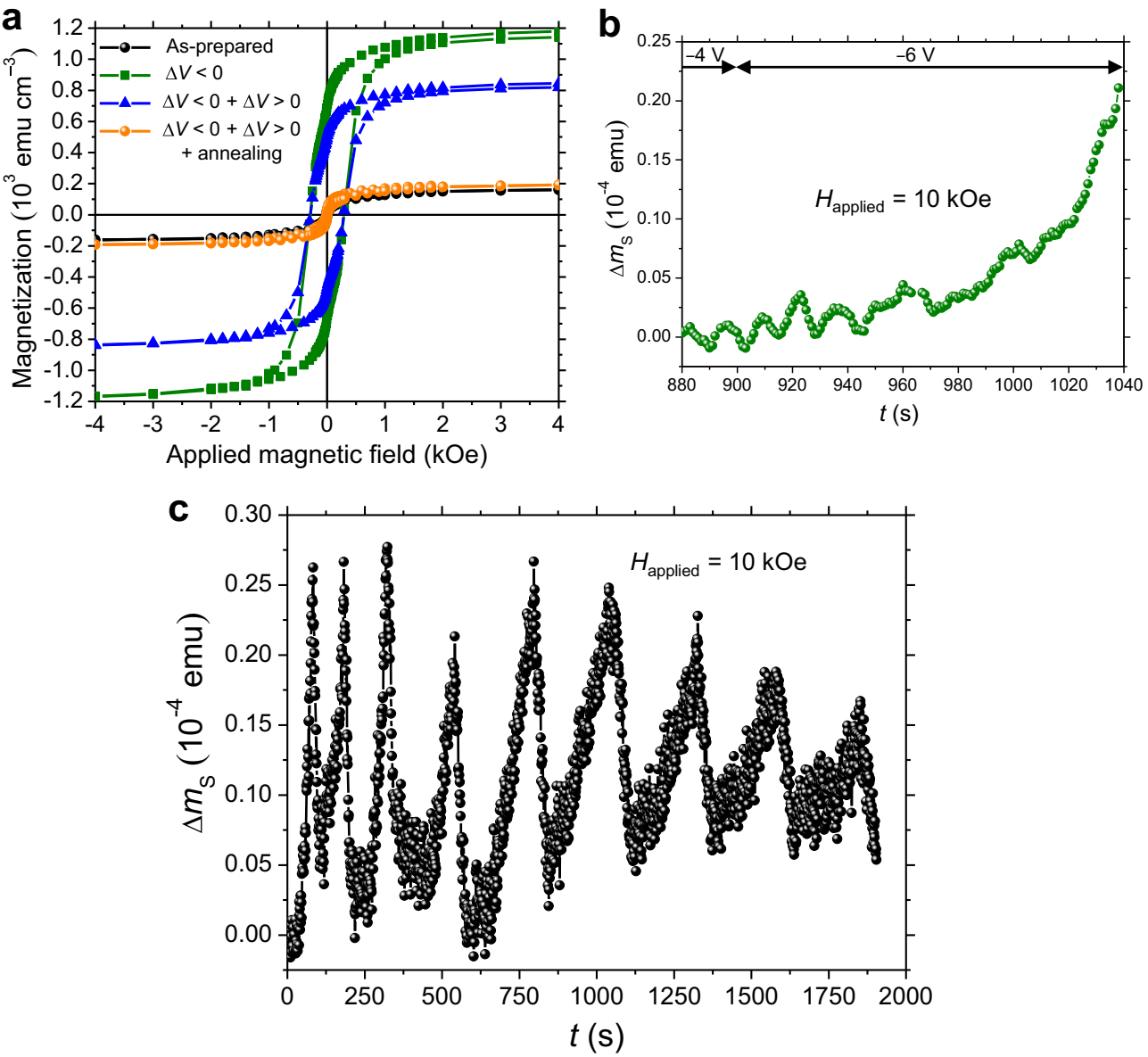


**Fig. 4 | Reversibility and cyclability. a** Hysteresis loops of the as-prepared (black), after being actuated with − 50 V for 1 h ($\Delta V < 0$) (green), upon − 50 V for 1 h ($\Delta V < 0$) and 50 V for 1 h ($\Delta V > 0$) (blue), and after − 50 V for 1 h ($\Delta V < 0$), 50 V for 1 h ($\Delta V > 0$) and annealing (orange). Note that he magnetization of the blue loop, recorded upon − 50 V for 1 h ($\Delta V < 0$)/50 V for 1 h ($\Delta V > 0$), is normalized to the volume of the voltage-treated sample and the magnetization of the orange loop, taken after − 50 V for 1 h ($\Delta V < 0$)/50 V for 1 h ($\Delta V > 0$)/annealing, is normalized to the volume of the as-prepared sample. **b** Onset voltage: Generated magnetic moment at saturation as a function of time while applying voltage in steps of 2 V, each for 5 min (*i.e.*, 0, − 2, − 4, and − 6 V). Only the magnetic moment at saturation during the first 140 s under −6 V is shown, as this voltage marks the onset of magneto-ionics. **c** Cyclability: Generated magnetic moment at saturation as a function of time while applying voltage pulses of −10 V/10 V for 60 s/20 s (1st cycle), 80 s/20 s (2nd cycle), 120 s/20 s (3rd cycle), 210 s/45 s (4th cycle), 210 s/45 s (5th cycle), and 210 s/60 s (for the 6th until the 10th cycle; the 10th cycle is not shown).

energies required to form a carbon vacancy in orthorhombic $Fe_2C$ and $Fe_3C$ are very low (0.085 and 0.118 eV/f.u., respectively) compared with the much higher energetic cost for inserting a carbon atom into BCC-Fe (1.104 eV/f.u.). This energetic landscape explains the facile decarburization of iron carbides into Fe-rich phases, while also rationalizing the difficulty of reversing the process by voltage alone, highlighting the critical role of Fe-C bonding in the observed magnetic reversibility. In addition, upon negative biasing, the overall electric behavior is less resistive (Supplementary Fig. S3), likely because of a highly defective voltage-driven C-rich layer (area V of Fig. 2c, d), limiting the reverse ionic process with voltages of opposite polarity. This indicates that the C-rich layer formed through voltage-induced means is more defective than those produced after annealing (*i.e.*, thermal treatment of the as-grown sample). Given the relatively large size of the heterostructures, pinhole formation is therefore more likely, and hence the resistance drops. Further, Fig. 4b shows that the onset voltage to induce voltage-driven motion of Fe and C, tracked by the generation of magnetic moment at saturation while gating, is −6 V, comparable to O-based magneto-ionics[8]. As seen in Fig. 4c, cyclability tests using voltage pulses of − 10 V/10 V indicate that the system is magnetically reversible and cyclable. In the first five − 10 V/10 V actuation sequences, the duration of the pulses was adjusted to achieve a similar generated magnetic moment. After the fifth loop, the pulse sequence is kept the same.

It is worth noting that this work represents a proof-of-principle study, providing to the best of our knowledge the foremost

demonstration of carbon as a viable magneto-ionic ion, while further optimization will be required to adapt the Fe-C system for practical applications. Specifically, although magnetic modulation was achieved under high gating voltages with partial reversibility, several strategies could enhance efficiency and cyclability. These include electrolyte engineering to increase conductivity[33] and decrease actuation voltages, the growth of protective top layers with higher carbon affinity, and post-treatments to tailor defects and off-stoichiometries within the heterostructure, such as ion implantation[34], to promote ion mobility back and forth and improve endurance.

With the goal of contextualizing the performance of carbon-based magneto-ionics within the research field of magneto-ionics, a two-step approach is followed:

a) **Comparison with other magneto-ionic systems with similar heterostructure design subjected to an analogous voltage protocol:** The current results are compared with those of liquid electrolyte gating, using propylene carbonate with $Na^+$ and $OH^-$ solvated species in ppm, $Co_3O_4$, CoN, CoMnN and CoFeN (Supplementary Table S1).

b) **Positioning the C-based magneto-ionics within a broader magneto-ionic landscape:** The performance of carbon magneto-ionics is contextualized alongside other reported magneto-ionic systems (*e.g.*, $O^{2-}$, $N^{3-}$, $H^+$, $Li^+$, $OH^-$). While direct one-to-one comparison is limited by differences in targeted magnetic properties and device configurations, a qualitative or semi-quantitative evaluation of the performance can illustrate key trends, such as typical diffusion coefficients, achievable magnetization modulation, and characteristic switching voltages, thereby emphasizing the novelty and technological relevance of C-ion-based magneto-ionic control (Supplementary Table S2).

In conclusion, when comparing magneto-ionics across diverse systems, C-based magneto-ionics exhibits performance comparable to that of oxygen-based magneto-ionics with slightly more limited reversibility, somewhat faster ion motion, higher induced magnetization and coercivity, and larger potential for biocompatibility[35–37].

Summarizing, our findings unambiguously demonstrate a planar-front voltage-driven dual-ion (C and Fe) transport as a means to reversibly control ferromagnetism in Fe-C-based heterostructures. This dual-ion movement leads to a large increase in saturation magnetization and coercivity with rather large magneto-ionic rates. Notably, since carbon, iron, and their carbides exhibit low cytotoxicity, this opens new possibilities for the integration of spintronics and biotechnology[35,36], such as brain-machine interfaces[37], offering a communication bridge between the brain's electrical activity and an external device.

## Methods

### Sample fabrication: growth of the heterostructure

45 nm-thick Fe-C thin films were grown at room temperature using DC and RF co-sputtering from Fe and C targets, respectively, on top of Si(001) wafers previously coated with a 15 nm-thick Ti adhesion layer and a 50 nm-thick Cu seed layer (to act as bottom electrode). Before depositing the Fe-C film, a portion of the Cu seed layer was masked to make electrical contacts for subsequent magneto-electric characterization (Fig. 1a). A 5 nm-thick layer of Ti-C was deposited on the Fe-C layer by co-sputtering of Ti and C targets using DC and RF powering, respectively, to serve as a carbon ion reservoir and as protective layer, against both oxidation and the insertion of other ionic species from the liquid electrolyte during gating. In Supplementary Figs. S15, S16, while the O signal originates from passivation (*i.e.*, natural oxidation) of the metallic components after exposure of the TEM lamella to air, the N signal arises from an artifact of spectral overlap of N $K_\alpha$ + Ti $L_\lambda$ peaks. However, upon gating, traces of Na ( ≤ 1 at. %; Supplementary Figs. S15, S16) are observed only in the upper part of the biased heterostructures (Area V). Since the Na concentration in the lower part ($Fe_{80}C_{20}$, Area VI), responsible for the magnetic signal, is virtually negligible, the effect of Na on the magnetic properties is expected to be minimal. Moreover, note that due to the gating polarity, $OH^-$ ions from the electrolyte cannot penetrate into the sample. The stronger affinity of carbon for Ti relative to Fe promotes the segregation of Fe and C during annealing, leading to a layered structure with distinct Fe-to-C ratios. This configuration enhances the overall out-of-plane resistivity of the heterostructure, thereby facilitating voltage-driven Fe and C transport and enabling magneto-ionic functionality. The substrate-to-target distance was approximately 10 cm. The base pressure of the system was around $8\times10^{-8}$ Torr. The depositions were carried out in an AJA International, Inc. ATC 2000-V Sputtering System. Subsequently, the films were annealed in a tubular furnace at 300 °C for 2 h under a controlled atmosphere of 95 % Ar and 5 % $H_2$ at a total flow rate of 80 sccm (flow percentages). The heating and cooling rates were 3 °C/min. See Supplementary Section 1 and Supplementary Fig. S1 for further details on the fabrication of the as-prepared heterostructure. The as-grown samples after annealing are denoted as "as-prepared" throughout the manuscript.

### Magneto-electric characterization

Magnetic measurements were carried out using a vibrating sample magnetometer (VSM) from MicroSense (LOT, Quantum Design). Magneto-electric measurements were done by performing VSM measurements while applying voltage through a custom-made electrolytic cell (Supplementary Fig. S2). Liquid electrolyte gating of the samples was achieved using an external Agilent B2902A power supply, applying voltage across the counter electrode (a Pt wire) and the working electrode (*i.e.*, the Cu bottom electrode). The electrolyte utilized was anhydrous propylene carbonate solvating $Na^+$ and $OH^-$ species (10 − 25 ppm), generated through the immersion of metallic sodium pieces capable of reacting with any residual water traces[8,11,12]. Liquid electrolyte was selected over solid-state gating because it enables the generation of sufficiently strong electric fields with moderate voltages, through the formation of an ultra-thin electric double layer at the electrolyte/heterostructure interface, to drive ion transport, while also allowing reliable characterization of large-area heterostructures without the risk of electrical shortcuts. Typically, the electric fields generated in solid-state configurations are considerably smaller than for liquid electrolyte actuation, leading to weaker magneto-ionic effects. Moreover, given the proof-of-principle nature of this study, large-area samples are necessary to probe substantial material volumes and to comprehensively assess the magneto-ionic effects from magnetic, electric, magnetoelectric, and structural perspectives, thereby allowing to elucidate the ion transport mechanisms behind the observed effects.

Since both the fabrication of the as-prepared sample and the voltage treatment result in an increased thickness (Supplementary Fig. S6 and Supplementary Section 3), the magnetization values are determined by normalizing the magnetic moment to the volume of Fe-containing layers, and the magnetic moment at saturation is plotted instead of saturation magnetization in Fig. 1c. In the as-grown sample and in the as-prepared heterostructure, Fe is irregularly distributed within the C matrix across the entire Fe-C layer, leading to underestimated magnetization values because the volume used for normalizing the magnetic moment includes the non-ferromagnetic C-rich regions. In contrast, the voltage-actuated heterostructure exhibits a more localized Fe distribution, enabling more accurate normalization with minimal contribution from non-ferromagnetic phases, and thus yielding magnetization values that are more representative. Supplementary Fig. S6 plots the magnetic data using the magnetic moment to avoid misinterpretations driven by volume normalization of the magnetic moment to obtain magnetization.

All samples are of the same area (0.3 $cm^2$). The thickness of as-grown, as-prepared, and voltage-treated samples are 45, 58, and

68 nm, respectively (Supplementary Fig. S4), while the thicknesses of Fe containing layers of these heterostructures are 45, 58, and 23 nm, respectively (thickness of Area VI since Area V is virtually Fe-free, Supplementary Figs. S4, S12). Hence, the volume of Fe-containing layers is $13.5 \times 10^{-7}$, $17.4 \times 10^{-7}$, and $6.9 \times 10^{-7}$ $cm^3$, respectively. The saturation magnetization values were taken at an applied magnetic field of 10 kOe, which is sufficiently high to ensure full saturation of the involved magnetic phases. For the time-dependent measurements, the field was fixed at 10 kOe. The maximum applied fields for the hysteresis loops were 20 kOe. Linear slopes in the hysteresis loops at applied magnetic fields far above the saturation field of the involved ferromagnetic phases were subtracted to remove the diamagnetic and paramagnetic contributions of the non-ferromagnetic contributions, *e.g.*, substrate, buffer and capping layers, and paramagnetic Fe-C phases. All the magnetic fields were applied along the film plane direction (*i.e.*, in-plane measurements).

### Structural and compositional characterizations

Cross-sectional lamellae, obtained by focused ion beam, of the investigated heterostructures were characterized by transmission electron microscopy (TEM). Specifically, TEM, high-resolution TEM, high-angle annular dark-field scanning transmission electron microscopy (HAADF-STEM), and electron energy loss spectroscopy (EELS) of Fig. 2, Supplementary Fig. S1a–c, and Supplementary Fig. S4 were carried out on a TECNAI F20 HRTEM/STEM microscope operated at 200 kV. High-resolution TEM of Supplementary Figs. S11, S12, and energy-dispersive X-ray (EDX) analysis (not shown) were performed on a Spectra 300 (S) TEM microscope operated at 200 kV in the Joint Electron Microscopy Center at ALBA Synchrotron. For the cross-sectional lamellae preparation by focused ion beam, an electrically conducting Pt-C is deposited on top of the heterostructures to enhance electrical conductivity (and to minimize charging effects), to protect them from oxidation and contamination, and to improve the quality of the final thin section since it prevents ion beam damage. Note that the quantification of Ti-C layer composition using EDX may be influenced by the carbon present in the adjacent Pt-C layer used for the lamella preparation. While the observed trend in carbon concentration changes within the Ti-C layers during annealing and voltage actuation is reliable, the absolute values should be interpreted as approximate values. Moreover, given that the composition quantification by EDX was performed over a relatively small area (approximately 400 $nm^2$), the reported compositions should be considered approximate yet representative. A similar limitation applies to the color intensity in the elemental EELS mappings, where only simultaneously recorded mapping images should be compared.

X-ray absorption spectroscopy (XAS) at the Fe $L_{2,3}$ edges was carried out at the BL29-BOREAS beamline at the ALBA Synchrotron[38]. The spectra were obtained using both total electron yield (TEY) and fluorescence yield (FY) modes at room temperature (300 K).

Defect characterization was carried out by variable energy positron annihilation lifetime spectroscopy (VEPALS). VEPALS measurements were conducted at the Mono-energetic Positron Source (MePS) beamline at Helmholtz-Zentrum Dresden – Rossendorf (Germany)[39]. A $CeBr_3$ scintillator detector, together with a Hamamatsu R13089-100 photomultiplier tube for the gamma photons detection was employed. A Teledyne SPDevices ADQ14DC-2X digitizer with a 14-bit vertical resolution and 2GS/s (gigasamples per second) horizontal resolution was utilized for the processing of signals. The overall time resolution of the measurement system is ≈ 0.250 ns and all spectra contain at least $1 \times 10^7$ counts. A typical lifetime spectrum $N(t)$, which is the absolute value of the time derivative of the positron decay spectrum, is described by $N(t) = R(t)^* \sum_{i=1}^{k+1} \frac{I_i}{\tau_i} e^{-t/\tau_i} + \text{Background}$, where k is the number of different defect types contributing to the positron trapping, which are related to k + 1 components in the spectra with individual lifetimes $\tau_i$ and intensities $I_i$ ($\sum I_i = 1$). The instrument resolution function $R(t)$ is a sum of two Gaussian functions with distinct intensities and relative shifts, both depending on the positron implantation energy, $E_P$. It was determined by measuring a reference sample, i.e., yttria-stabilized zirconia, which exhibits a known single lifetime component of 182 ± 3 ps. The background was negligible. All the spectra were deconvoluted using a non-linear least-squares fitting method, minimized by the Levenberg-Marquardt algorithm in the software package PALSfit[40], into 2 major lifetime components, which directly evidence localized annihilation at 2 different defect types (sizes; $\tau_1$ and $\tau_2$). The corresponding relative intensities largely reflect the concentration of each defect type (size) if the size of the compared defects is in a similar range. In general, positron lifetime is directly proportional to defects size, *i.e.*, the larger the open volume is, the lower the probability there is for positrons to be annihilated with electrons, and thereby the longer positron lifetime[41]. The positron lifetime and its intensity have been probed as a function of positron implantation energy $E_P$ which can be recalculated to the mean positron implantation depth $\langle z \rangle$ using: $\langle z \rangle\,(\text{nm}) = \frac{23.9}{\rho\left(\frac{g}{cm^3}\right)} E_P(\text{keV})^{1.69}$[42], which is an approximate measurement of depth since it does not account for positron diffusion. The orange background of Fig. 3, which approximates the Fe-C film region, is calculated using this formula and assuming the density of $Fe_3C$[18] for the Fe-C film. The average positron lifetime $\tau_{Av}$ is defined as $\tau_{Av} = \sum \tau_i I_i$, and it has a high sensitivity to the defect size (or type).

### Electrical characterization

For the electrical actuation across the as-prepared heterostructures, voltages were applied through a TFAnalyser3000 platform (aixACCT Systems GmbH) between the bottom electrode and a probe tip that was in contact with the sample surface. The presented current intensity *vs.* applied voltage curves were obtained from averaging the datasets recorded on ten different areas of the surface of the heterostructures using 2 s integration time.

### Broadband ferromagnetic resonance spectroscopy

Broadband ferromagnetic resonance spectroscopy (BFMR) measurements are performed using a homemade setup consisting of a commercial electromagnet and a vector network analyzer (VNA) combined with a grounded coplanar waveguide (GCPW). The sample is positioned face down on the GCPW, in the "flip-chip" configuration, where the radio frequency current generated by the VNA is converted into an oscillatory magnetic field on the sample. The quasi-static external magnetic field ($H_{ext}$) generated by the electromagnet is applied parallel to the thin film sample surface, and perpendicular to the oscillatory magnetic field[43,44].

### Ab initio calculations

Our first-principles calculations are based on the projector-augmented wave (PAW) method[45] as implemented in the VASP package[46] using the generalized gradient approximation[47]. The orthorhombic unit cells of $Fe_2C$ and $Fe_3C$ as well as BCC-Fe were considered. The atomic coordinates as well as the volume of the unit cells were relaxed until the forces became smaller than 1 meV/Å. We found the following lattice parameters: $Fe_2C$ (a = 2.823 Å, b = 4.276 Å, c = 4.708 Å); $Fe_3C$ (a = 4.478 Å, b = 5.032 Å, c = 6.722 Å) and BCC-Fe (a = 2.83 Å). A kinetic energy cutoff of 550 eV has been used for the plane-wave basis set, and Γ-centered 35×23×21, 25×23×17, 35×35×35 k-meshes were used to sample the first Brillouin zone of $Fe_2C$, $Fe_3C$, and Fe, respectively. The formation energies were calculated using the elemental unit cells of the carbides, graphite, and BCC iron. van der Waals forces were included with Grimme-type dispersion-corrected density functional theory-D2[48] to properly describe the electronic structure of graphite.

## Data availability

The authors declare that the data supporting the findings of this study are available within the paper and its supplementary information files. Source data have been deposited in the Figshare database under the accession code: https://doi.org/10.6084/m9.figshare.30910850.

## References


1. Nichterwitz, M. et al. Advances in magneto-ionic materials and perspectives for their application. *APL Mater.* **9**, 030903 (2021).
2. Leighton, C., Birol, T. & Walter, J. What controls electrostatic vs electrochemical response in electrolyte-gated materials? A perspective on critical materials factors. *APL Mater.* **10**, 040901 (2022).
3. Mishra, R., Kumar, D. & Yang, H. Oxygen-migration-based spintronic device emulating a biological synapse. *Phys. Rev. Appl.* **11**, 054065 (2019).
4. Ye, X. et al. Selective dual-ion modulation in solid-state magnetoelectric heterojunctions for in-memory encryption. *Small* **19**, 448–452 (2023).
5. Tan, A. J. et al. Magneto-ionic control of magnetism using a solid-state proton pump. *Nat. Mater.* **18**, 35–41 (2019).
6. Ameziane, M. et al. Lithium-ion battery technology for voltage control of perpendicular magnetization. *Adv. Funct. Mater.* **32**, 2113118 (2022).
7. Bauer, U. et al. Magneto-ionic control of interfacial magnetism. *Nat. Mater.* **14**, 174–181 (2015).
8. Quintana, A. et al. Voltage-controlled ON-OFF ferromagnetism at room temperature in a single metal oxide film. *ACS Nano* **12**, 10291–10300 (2018).
9. Vasala, S. et al. Reversible tuning of magnetization in a ferromagnetic Ruddlesden–Popper-type manganite by electrochemical fluoride-ion intercalation. *Adv. Electron. Mater.* **6**, 1900974 (2020).
10. Quintana, A. et al. Hydroxide-based magneto-ionics: electric-field control of a reversible paramagnetic-to-ferromagnetic switch in α-$Co(OH)_2$ films. *J. Mater. Chem. C* **10**, 17145–17153 (2022).
11. de Rojas, J. et al. Voltage-driven motion of nitrogen ions: a new paradigm for magneto-ionics. *Nat. Commun.* **11**, 5871 (2020).
12. de Rojas, J. et al. Critical role of electrical resistivity in magnetoionics. *Phys. Rev. Appl.* **16**, 034042 (2021).
13. Jensen, C. J. et al. Nitrogen-Based Magneto-ionic Manipulation of Exchange Bias in CoFe/MnN Heterostructures. *ACS Nano* **17**, 6745–6753 (2023).
14. Jeong, J., Park, Y. S., Kang, M.-G. & Park, B.-G. Nanosecond magneto-ionic control of magnetism using a resistive switching $HfO_2$ gate oxide. *Adv. Electron. Mater.* **10**, 2400535 (2024).
15. Lv, Z. Q., Sun, S. H., Jiang, P., Wang, B. Z. & Fu, W. T. First-principles study on the structural stability, electronic and magnetic properties of $Fe_2$. *C. Comput. Mater. Sci.* **42**, 692–697 (2008).
16. Tsuzuki, A., Sago, S., Lu, J., Hirano, S.-I. & Naka, S. High temperature and pressure preparation and properties of iron carbides $Fe_7C_3$ and $Fe_3C$. *J. Mater. Sci.* **19**, 2513–2518 (1984).
17. Jain, A. et al. Commentary: the Materials Project: a materials genome approach to accelerating materials innovation. *APL Mater.* **1**, 011002 (2013).
18. Bhadeshia, H. K. D. H. Cementite. *Inter. Mater. Rev.* **65**, 1–27 (2020).
19. Skomski, R. & Coey, J. M. D. *Permanent Magnetism* (Institute of Physics Publishing, 1999).
20. Shirzad, K. & Viney, C. A critical review on applications of the Avrami equation beyond materials science. *J. R. Soc. Interface* **20**, 20230242 (2023).
21. Kneller, E. F. & Luborsky, F. E. Particle size dependence of coercivity and remanence of single domain particles. *J. Appl. Phys.* **34**, 656–658 (1963).
22. Hadjipanayis, G. C. Nanophase hard magnets. *J. Magn. Magn. Mater.* **200**, 373–391 (1999).
23. Liu, D. et al. Giant magnetic coercivity in $Fe_3C$-filled carbon nanotubes. *RSC Adv.* **8**, 13820 (2018).
24. Kneller, E. F. & Luborsky, F. E. Particle Size Dependence of Coercivity and Remanence of Single-Domain Particles. *J. Appl. Phys.* **34**, 656–658 (1963).
25. Anand, M. Anisotropic effect of dipolar interaction in ordered ensembles of nanoparticles. *J. Nanopart. Res.* **24**, 53 (2022).
26. Hong, J. Thickness-dependent magnetic anisotropy in ultrathin Fe/Co/Cu(001) films. *Phys. Rev. B* **74**, 172408 (2006).
27. Farle, M. Ferromagnetic resonance of ultrathin metallic layers. *Rep. Prog. Phys.* **61**, 755–826 (1998).
28. Kuanr, B. K., Veerakumar, V., Kuanr, A. V., Camley, R. E. & Celinski, Z. Effect of temperature on the ferromagnetic-resonance field and line width of epitaxial Fe thin films. *IEEE Trans. Magn.* **45**, 4015–4018 (2009).
29. Urquhart, K. B., Heinrich, B., Cochran, J. F., Arrott, A. S. & Myrtle, K. Ferromagnetic resonance in ultrahigh vacuum of bcc Fe(001) films grown on Ag(001). *J. Appl. Phys.* **64**, 5334–5336 (1988).
30. Sakamaki, M. & Amemiya, K. Nanometer-resolution depth-resolved measurement of florescence-yield soft x-ray absorption spectroscopy for FeCo thin film. *Rev. Sci. Instrum.* **88**, 083901 (2017).
31. Furlan, A., Jansson, U., Lu, J., Hultman, L. & Magnuson, M. Structure and bonding in amorphous iron carbide thin films. *J. Phys.: Condens. Matter.* **27**, 045002 (2015).
32. de Rojas, J. et al. Boosting room-temperature magneto-ionics in a non-magnetic oxide semiconductor. *Adv. Funct. Mater.* **30**, 2003704 (2020).
33. Martins, S. et al. Enhancing magneto-ionic effects in cobalt oxide films by electrolyte engineering. *Nanoscale. Horiz.* **8**, 118–126 (2023).
34. Ma, Z. et al. Controlling magneto-ionics by defect engineering through light ion implantation. *Adv. Funct. Mater.* **34**, 2312827 (2024).
35. Kim, S.-B., Kim, C.-H., Lee, S.-Y. & Park, S.-J. Carbon materials and their metal composites for biomedical applications: a short review. *Nanoscale* **16**, 16313–16328 (2024).
36. Yu, J. et al. Iron carbide nanoparticles: an innovative nanoplatform for biomedical applications. *Nanoscale Horiz* **2**, 81–88 (2017).
37. Li, J. et al. Sensing and stimulation applications of carbon nanomaterials in implantable brain-computer interface. *Int. J. Mol. Sci.* **24**, 5182 (2023).
38. Barla, A. et al. Design and performance of BOREAS, the beamline for resonant X-ray absorption and scattering experiments at the ALBA synchrotron light source. *J. Synchrotron Rad.* **23**, 1507–1517 (2016).
39. Wagner, A., Butterling, M., Liedke, M. O., Potzger, K. & Krause-Rehberg, R. Positron annihilation lifetime and Doppler broadening spectroscopy at the ELBE facility. *AIP Conf. Proc.* **1970**, 040003 (2018).
40. Olsen, J. V., Kirkegaard, P., Pedersen, N. J. & Eldrup, M. PALSfit: A new program for the evaluation of positron lifetime spectra. *Phys. Stat. Sol.* **4**, 4004–4006 (2007).
41. Tuomisto, F. & Makkonen, I. Defect identification in semiconductors with positron annihilation: experiment and theory. *Rev. Mod. Phys.* **85**, 1583–1631 (2013).
42. Dryzek, J. & Horodek, P. GEANT4 simulation of slow positron beam implantation profiles. *Nucl. Instrum. Methods Phys. Res. B* **266**, 4000–4009 (2008).
43. Longo, E. et al. Large spin-to-charge conversion at room temperature in extended epitaxial $Sb_2Te_3$ topological insulator chemically grown on silicon. *Adv. Funct. Mater.* **32**, 2109361 (2021).
44. Macià, F., Mirjolet, M. & Fontcuberta, J. Efficient spin pumping into metallic $SrVO_3$ epitaxial films. *J. Magn. Magn. Mater.* **546**, 168871 (2022).
45. Blöchl, P. Projector augmented-wave method. *Phys. Res. B* **50**, 17953–17979 (1994).

46. Kresse, G. & Hafner, J. Ab initio molecular dynamics for liquid metals. *Phys. Res. B* **47**, 558–561 (1993).
47. Perdew, J., Burke, K. & Ernzerhof, M. Generalized gradient approximation made simple. *Phys. Rev. Lett.* **77**, 3865–3868 (1996).
48. Bučko, T., Hafner, J., Lebègue, S. & Ángyán, J. Improved description of the structure of molecular and layered crystals: Ab Initio DFT Calculations with van der waals corrections. *J. Phys. Chem. A* **114**, 11814–11824 (2010).

## Acknowledgements

Financial support by the National Natural Science Foundation Research Funding, China, (Grant No. 52503312), Zhejiang Key Laboratory of Extreme Environment Functional Materials and the Zhejiang Provincial Postdoctoral Research Project First-Class Funding, China, (Grant No. ZJ2024029), European Union's Horizon 2020 Research and Innovation Program (BeMAGIC European Training Network, ETN/ITN Marie Skłodowska–Curie grant N° 861145), the DOCFAM-PLUS within HORIZON-MSCA-2021-COFUND-01 (grant N° 101081337), the European Research Council (2021-ERC-Advanced REMINDS Grant N° 101054687), the Spanish Government (PID2024-156385OB-I00, PID2023-150721OB-I00, PDC2023-145874-I00, PID2023-147211OB-C21 and CEX2023-001263-S), the Generalitat de Catalunya (2021-SGR-00651 and 2021-SGR-00804), the MCIN/AEI/10.13039/501100011033 & European Union NextGenerationEU/PRTR (grant N° CNS2022-135230), and France 2030 government grant managed by the French National Research Agency PEPR SPIN ANR-22-EXSP 0009 (SPINTHEORY), is acknowledged. ICN2 is funded by the CERCA program/Generalitat de Catalunya. The ICN2 is supported by the Severo Ochoa Centers of Excellence program, Grant CEX2021-001214-S, grant funded by MCIU/AEI/10.13039/501100011033. Authors acknowledge the use of instrumentation financed through Grant IU16-014206 (METCAM-FIB) to ICN2, funded by the European Union through the European Regional Development Fund (ERDF), with the support of the Ministry of Research and Universities, Generalitat de Catalunya. The XAS experiments were performed at BL29-BOREAS beamline at ALBA Synchrotron with the collaboration of ALBA staff under the in-house research proposal 2023027292. VEPALS were carried out at ELBE from the Helmholtz-Zentrum Dresden – Rossendorf e. V., a member of the Helmholtz Association. We would like to thank the facility staff for their assistance. We would also like to thank the Micro- and Nanofabrication Lab at Yiwu Research Institute for their technical support. E.M. is a Serra Húnter Fellow.

## Author contributions

E.M. had the original idea and led the investigation. Z.T. and E.M. designed the experiments. J.S. and E.M. supervised the work. Z.T., Z.M., E.P., and J.L.C.-K. synthesized the Fe-C films. Z.T., Z.M., S.P., and A.Q. carried out the magneto-electric measurements and analyzed the data. A.F.L., J.N., J.S., and E.M. applied the Avrami formalism to the time-dependent magneto-electric characterization. Z.T., Z.M., A.G.-T., and J.H.-M. carried out the XAS characterization and analyzed the data. Z.T., Y.F.M., X.Z.C., and A.A.-L. performed the TEM and STEM characterization and carried out the analysis of the corresponding data. Z.M., H.T., I.F., and F.S. performed the out-of-plane electrical measurements and analyzed the data. M.O.L., E.H., and A.W. characterized the samples by PALS and analyzed the data. F.I. and M.C. conducted the ab initio calculations. E.L., M.R., and F.M. performed the ferromagnetic resonance spectroscopy experiments and were responsible for data analysis and interpretation. All authors discussed the results and commented on the article. The article was written by Z.T., J.N., and E.M. with contributions from all co-authors.

## Competing interests

The authors declare no competing interests.

## Additional information

**Supplementary information** The online version contains supplementary material available at https://doi.org/10.1038/s41467-026-68283-w.

**Correspondence** and requests for materials should be addressed to Z. Tan, Z. Ma, J. Sort or E. Menéndez.

**Peer review information** *Nature Communications* thanks Hyeon Han, and the other anonymous reviewer(s) for their contribution to the peer review of this work. A peer review file is available.